Supplementary Information

Decoupled Green Hydrogen Production Using Platinum-Free Catalysts in a Bicarbonate Electrolyte

Luís Pinho, Mark Potter, Kathryn E. Toghill*

Department of Chemistry, Lancaster University, Lancaster, LA1 4YB, United Kingdom

*Corresponding Author: K.E. Toghill k.toghill@lancaster.ac.uk

Table S1. Summary of dual-circuit redox flow systems for decoupled water splitting.

pH	Anolyte	Catholyte	HER catalyst	OER catalyst	Reference number
1	V(III)/VII)	Ce (IV)/Ce(III)	Mo_2C	RuO_2	1
1	V(III)/VII)	Mn(III)/Mn(II)	Mo_2C	RuO_2	2
14	Fe(III)-TEA/Fe(II)-TEA	K_2MnO_4/ $KMnO_4$	10% Pt/C	N.A.	3
14	DHPS/DHPS-2H	Fe(III)/Fe(II)	$Pt/Ni(OH)_2$	$NiFe(OH)_2$	4

Table S2. Summary of candidate liquid redox mediator that can operate at near-neutral pH values in a dual-circuit redox flow system.

pH	Anolyte	Catholyte	Supporting electrolyte	Reference number
7	Methyl Viologen	7, 4-hydroxy-TEMPO	0.5 M NaCl	5

7	BTMAP-Vi	BTMAP-Fc	0.5 M NaCl	6
7	[Cr(f-DPA)2]Br	$K_4Fe(CN)_6$	1 M KCl	7
9	K_2VDTPA	K_3FeDTPA	0.1 M KBi	8

Table S3. Overpotentials at 10 mA cm^{-2} m and decoupled faradaic yields obtained for the electrocatalysts under study.

Electrocatalysts	**Overpotential at 10 mA cm^{-2}**	**Decoupled FY (%)**
V10Pt	208	60.29 ± 5.41
Ni APS	501	70.45 ± 8.35
MoS_2	542	93.39 ± 0.66
Mo_2C	565	65.975 ±1.95
Ni_xP_y	692	86.23 ± 6.29
Ni_xS_y	603	88.89 ± 4.77
CP	867	-

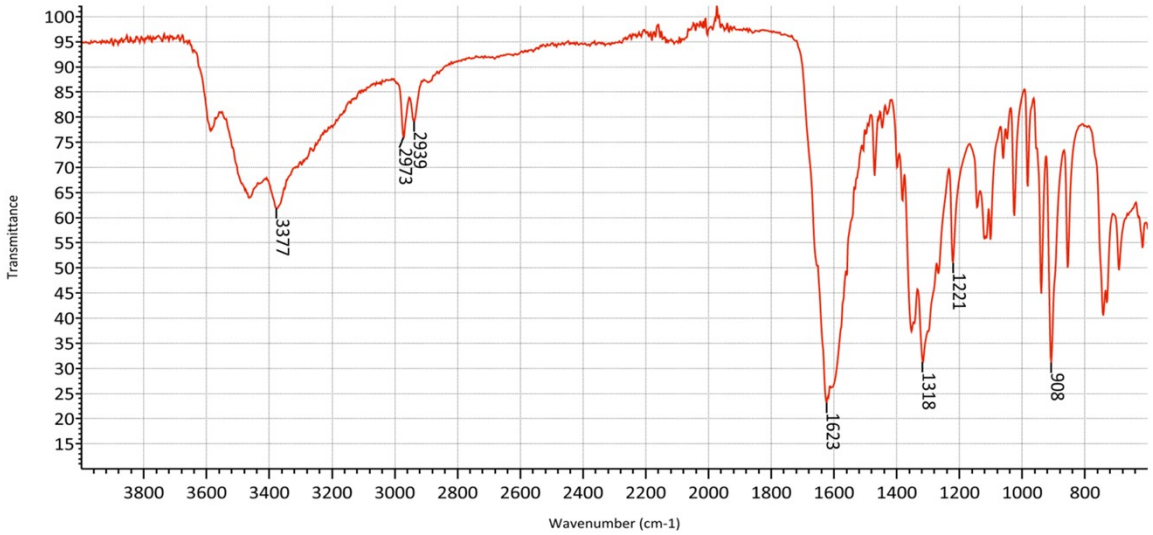

Figure S1. ATR-FTIR spectrum obtained for KCrPDTA.

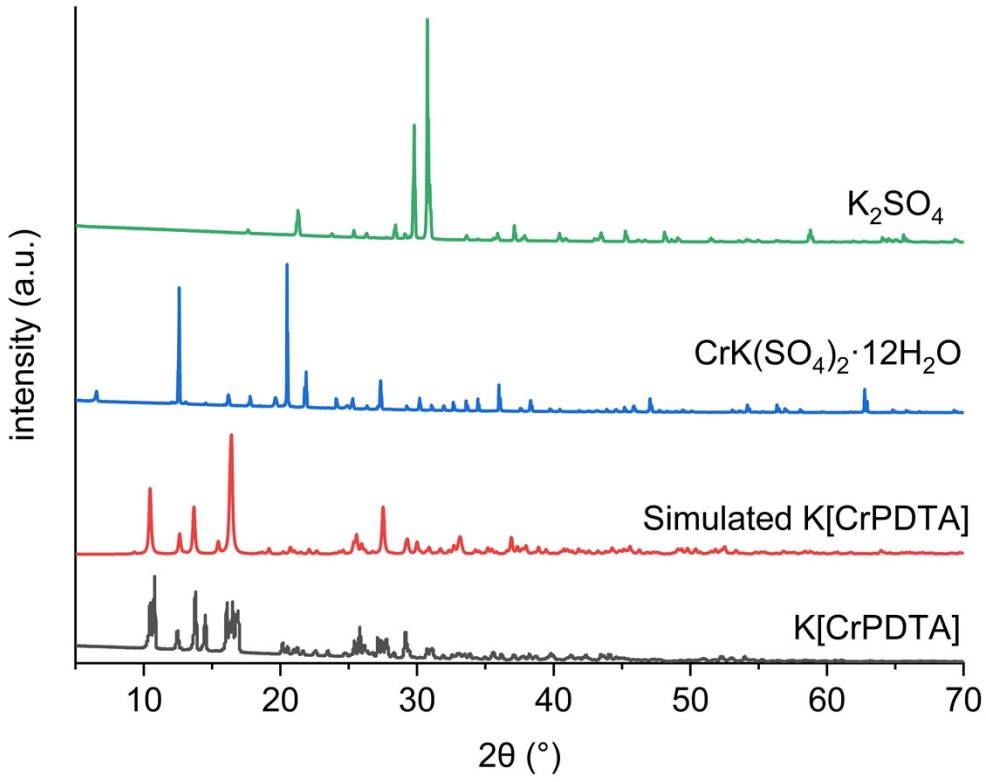

Figure S2. pXRD diffractograms obtained for KCrPDTA (experimental and simulated), $CrK(SO_4)_2.12H_2O$ and K_2SO_4.

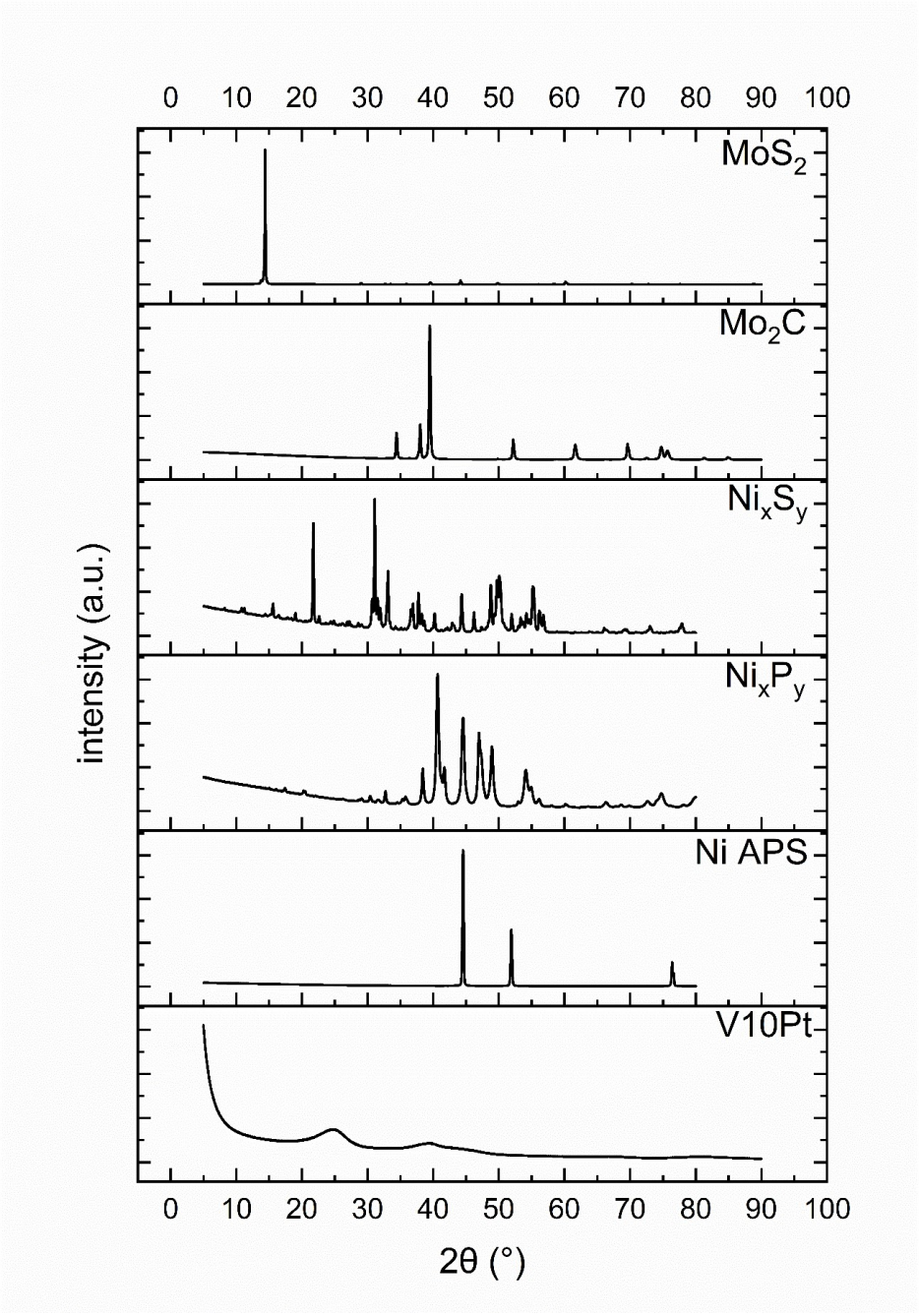

Figure S3. pXRD diffractograms obtained for MoS_2, Mo_2C, Ni_xS_y, Ni_xP_y, Ni APS and V10Pt electrocatalysts.

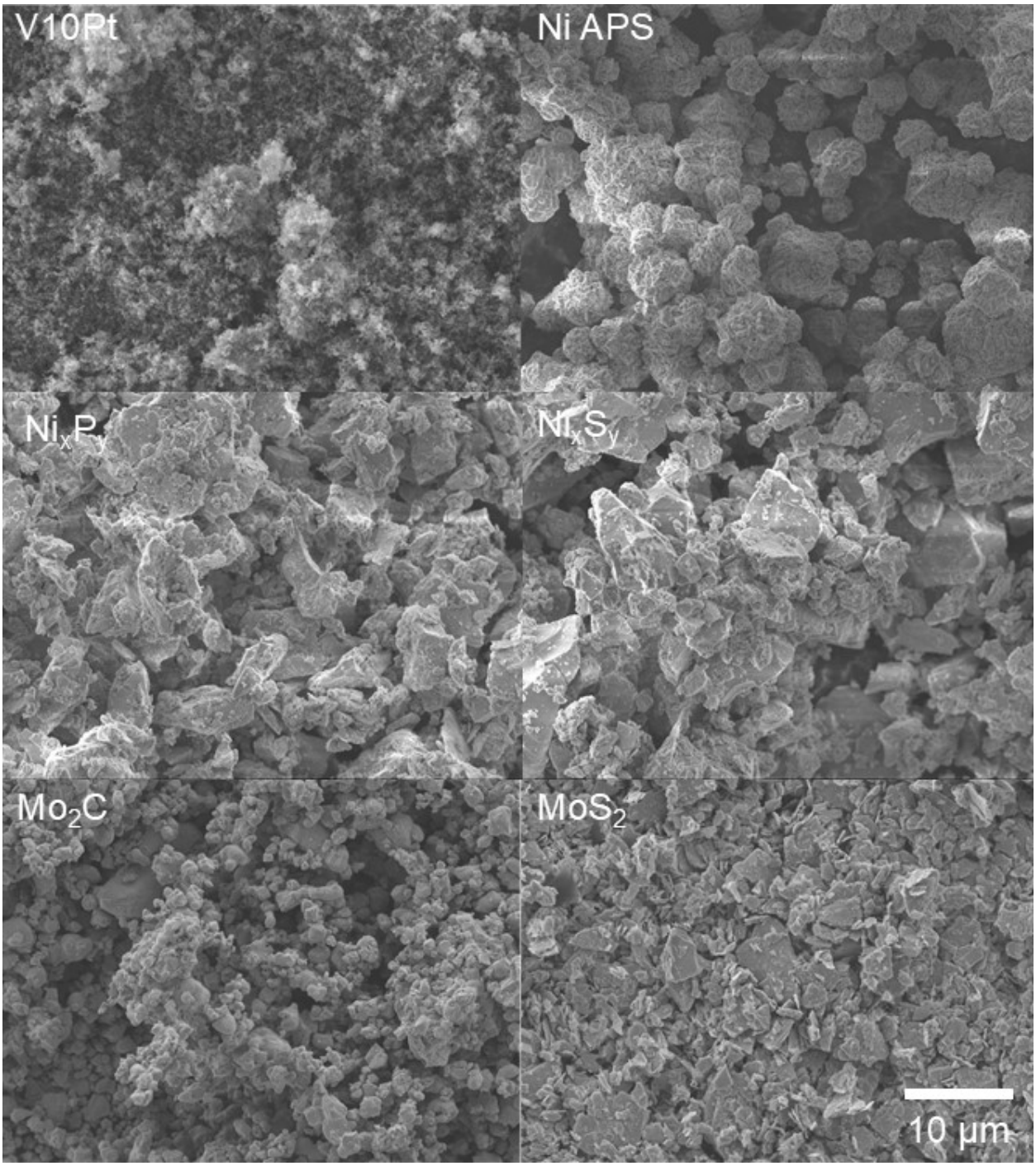

Figure S4. Lower magnification SEM images obtained for MoS_2, Mo_2C, Ni_xS_y, Ni_xP_y, Ni APS and V10Pt electrocatalysts.

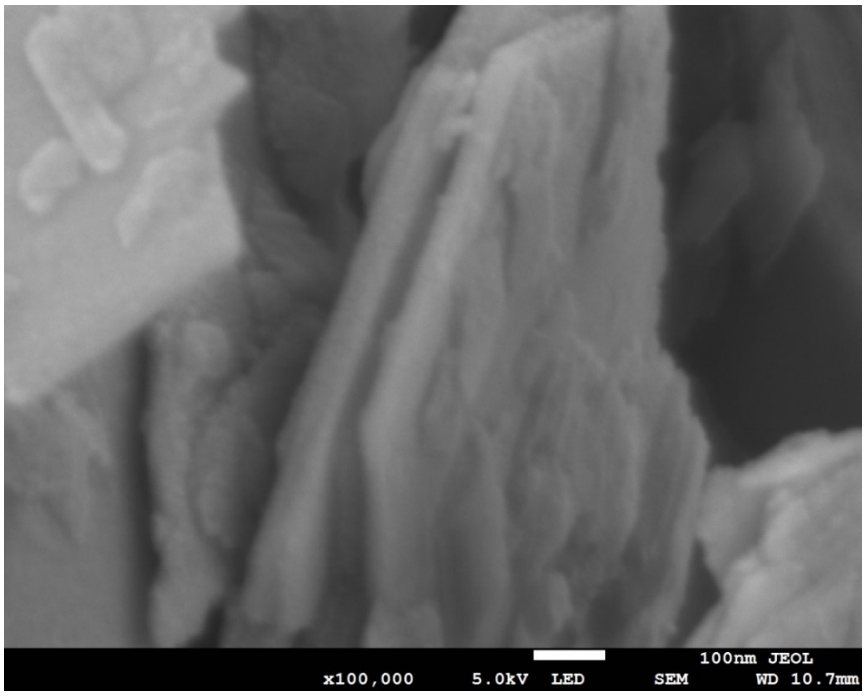

Figure S5. Higher magnification SEM image obtained for MoS_2 electrocatalyst.

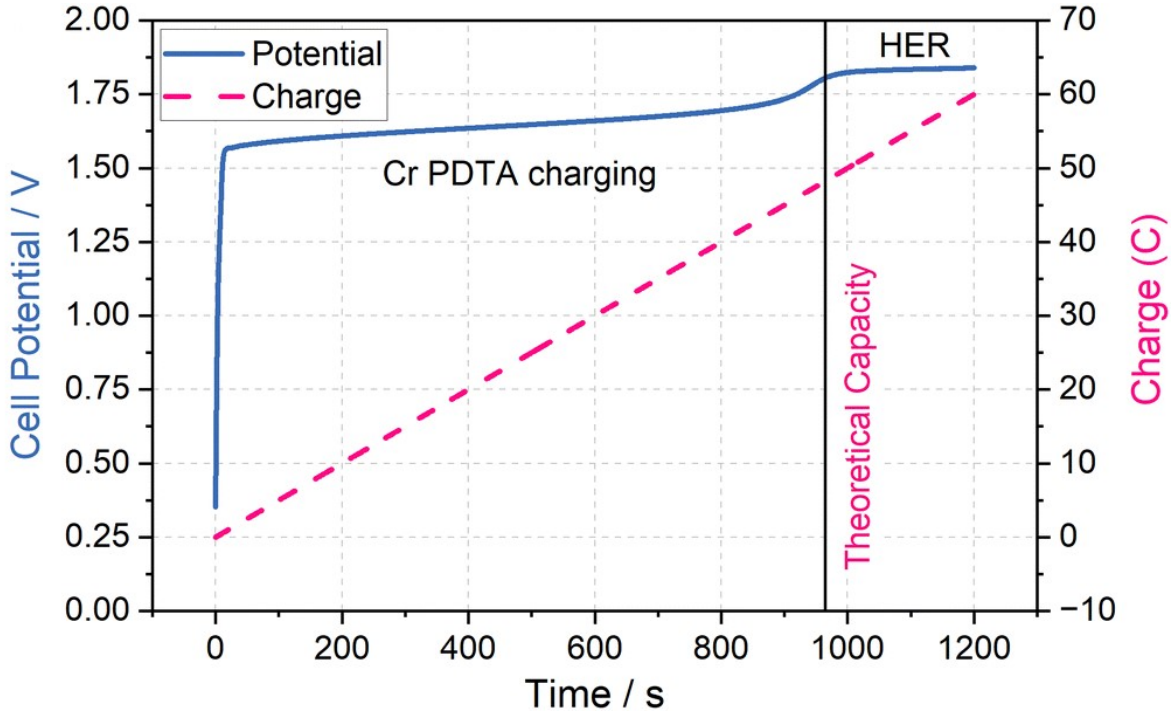

Figure S6. Galvanostatic charging profile of 10 mM Cr PDTA with 1 M $KHCO_3$ supporting electrolyte against excess $K_4Fe(CN)_6$ at 100 mA (electrode surface area 16 cm^2, Sigracell GFD 4.6). The potential (solid blue) and charge passed (dashed pink) are plotted with respect to time, with the line at x = 965 s indicating the theoretical capacity (48.25 C) of the 50 mL of 10 mM Cr PDTA charged during the experiment.

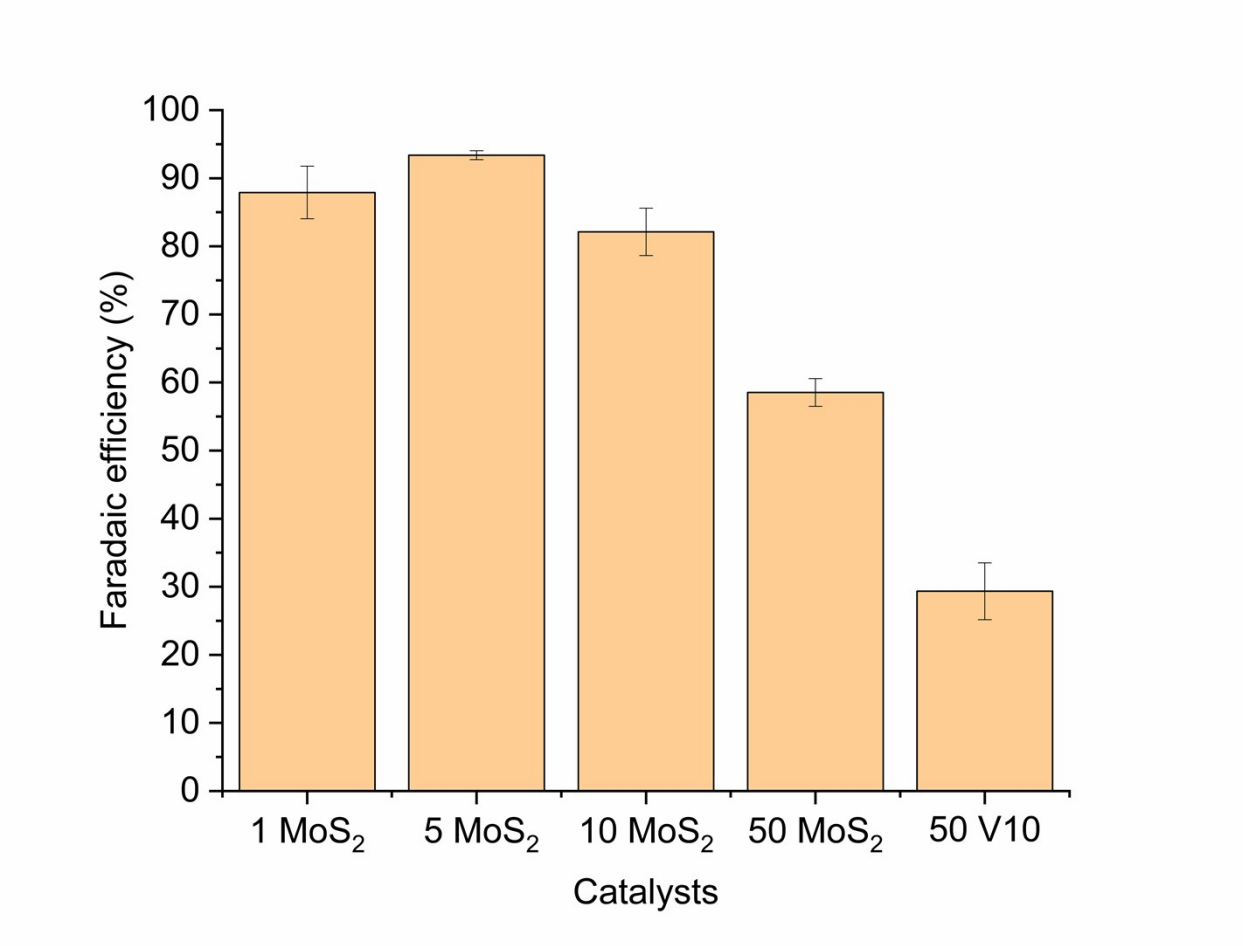

Figure S7. Faradaic yield for hydrogen and increasing concentrations (MoS_2 and V10Pt) electrocatalysts. Numbers in prefix indicate mg of electrocatalyst against 10 mM CrPDTA in 1M $KHCO_3$.

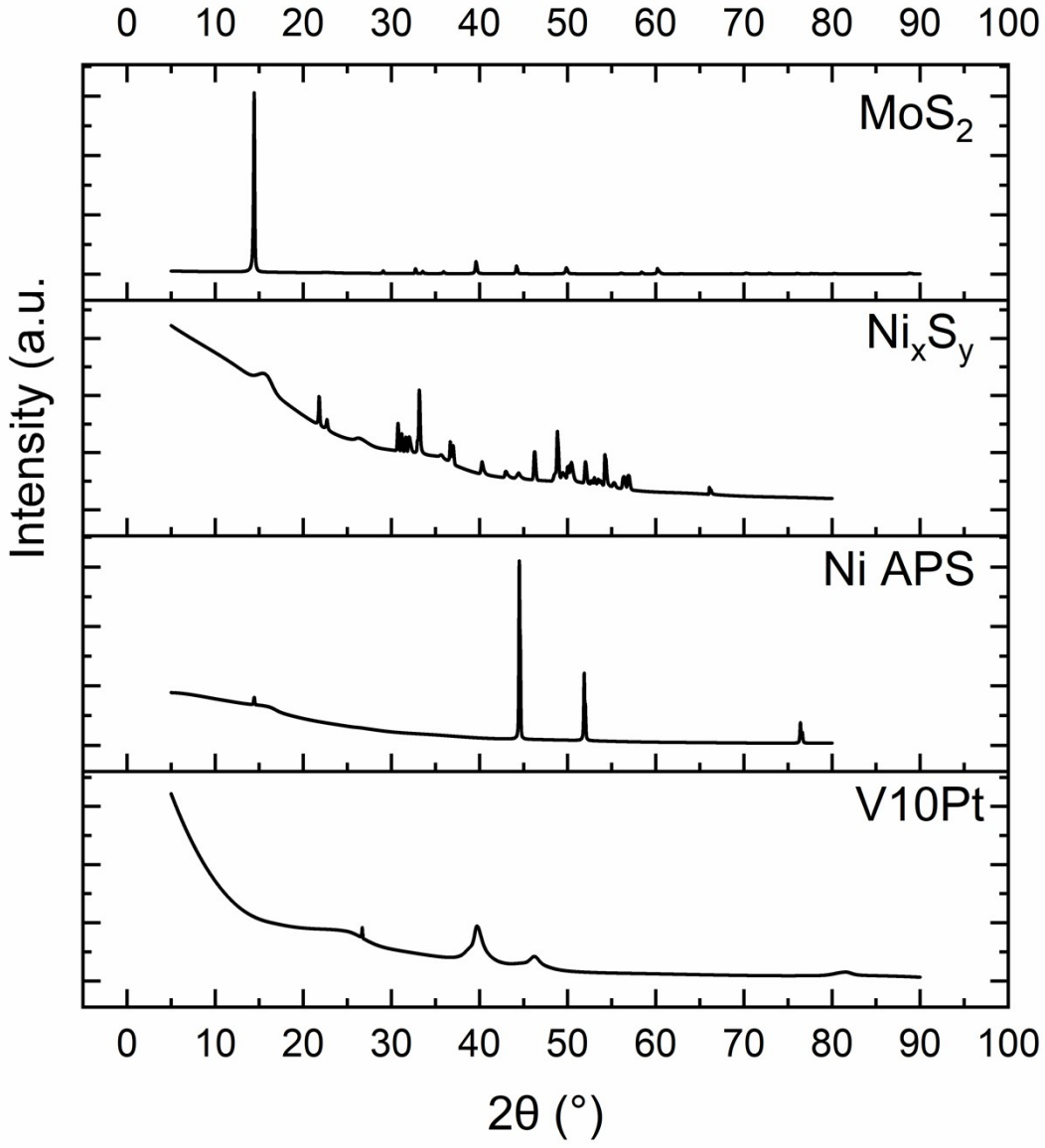

Figure S8. XRD of spent MoS_2, Ni_xS_y, Ni APS and V10Pt electrocatalysts. Information for Mo_2C and Ni_xP_y could not be obtained because these catalyst powders could not be separated from the mixture.

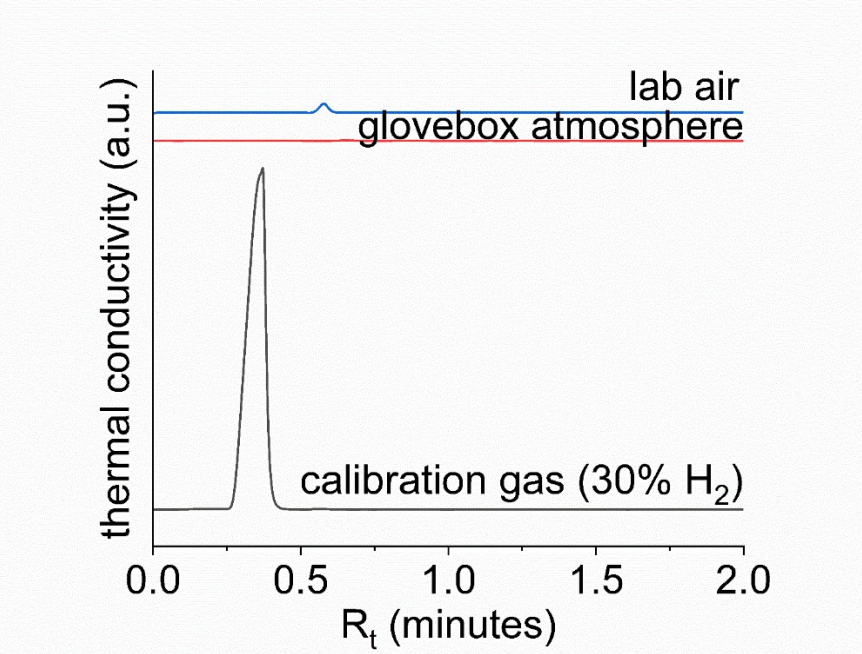

Figure S9. Representative gas chromatograms obtained for laboratory air, glovebox atmosphere and 30% H_2 in balance N_2 calibration gas.

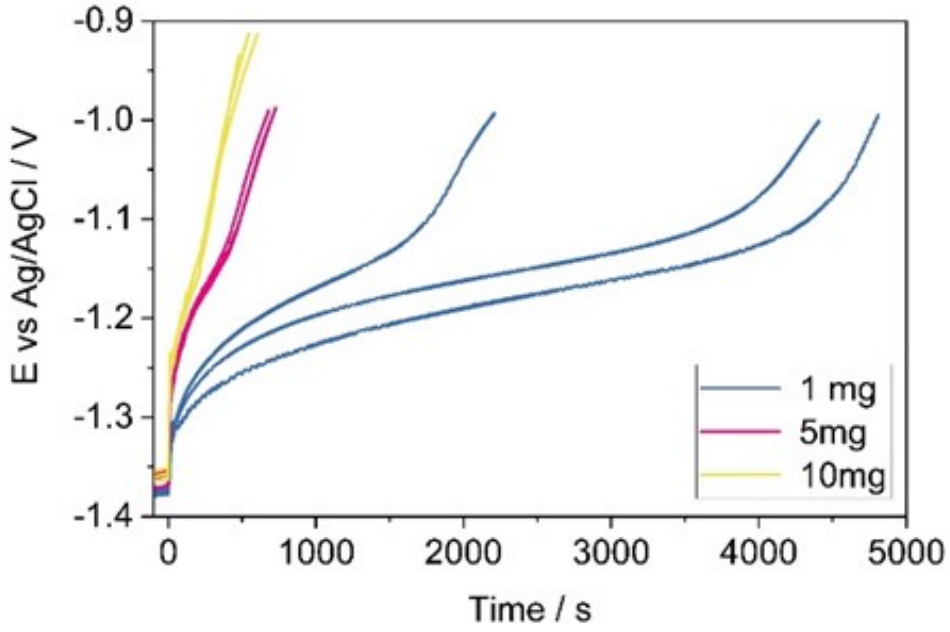

Figure S10. OCCP measurements for increasing MoS_2 concentrations. The charged mediator was left under stirring while OCP measurements were continuously taken. Initial time corresponds to the moment in which the MoS_2 dispersion was added. Initially, OCP values change very quickly upon the addition of catalyst at t_0 as charge was transferred onto the catalyst, followed by a slower slope controlled by the rate of HER.

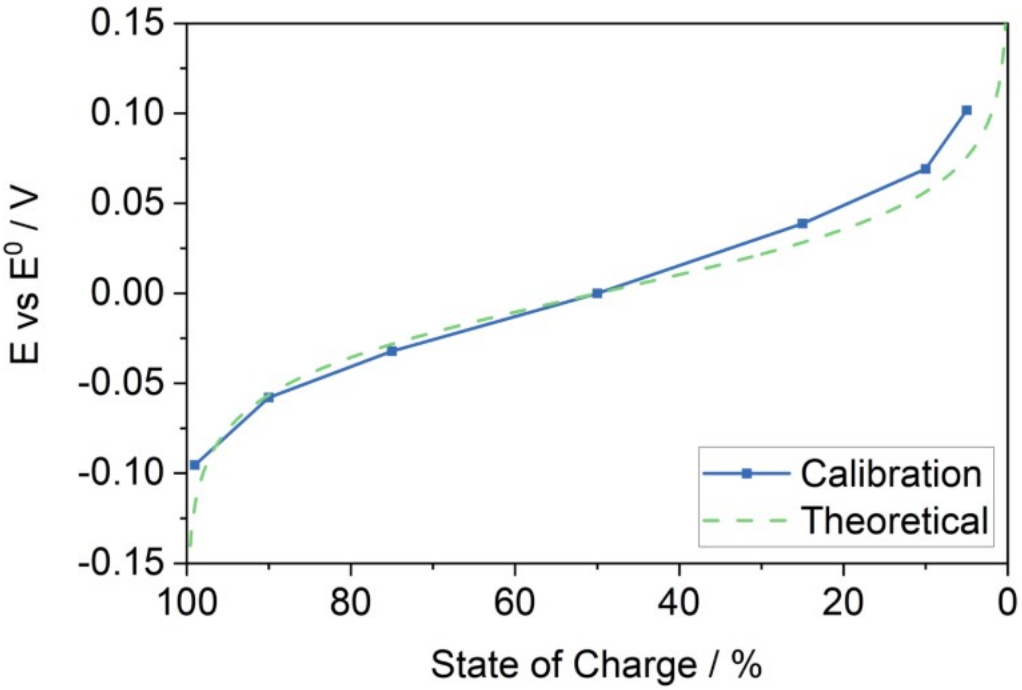

Figure S11. Open circuit potentials for states of charge of solutions of 10 mM Cr(II)/(III) PDTA where the state of charge indicates the % Cr(II) contributes to the overall concentration. A theoretical curve is included for comparison.

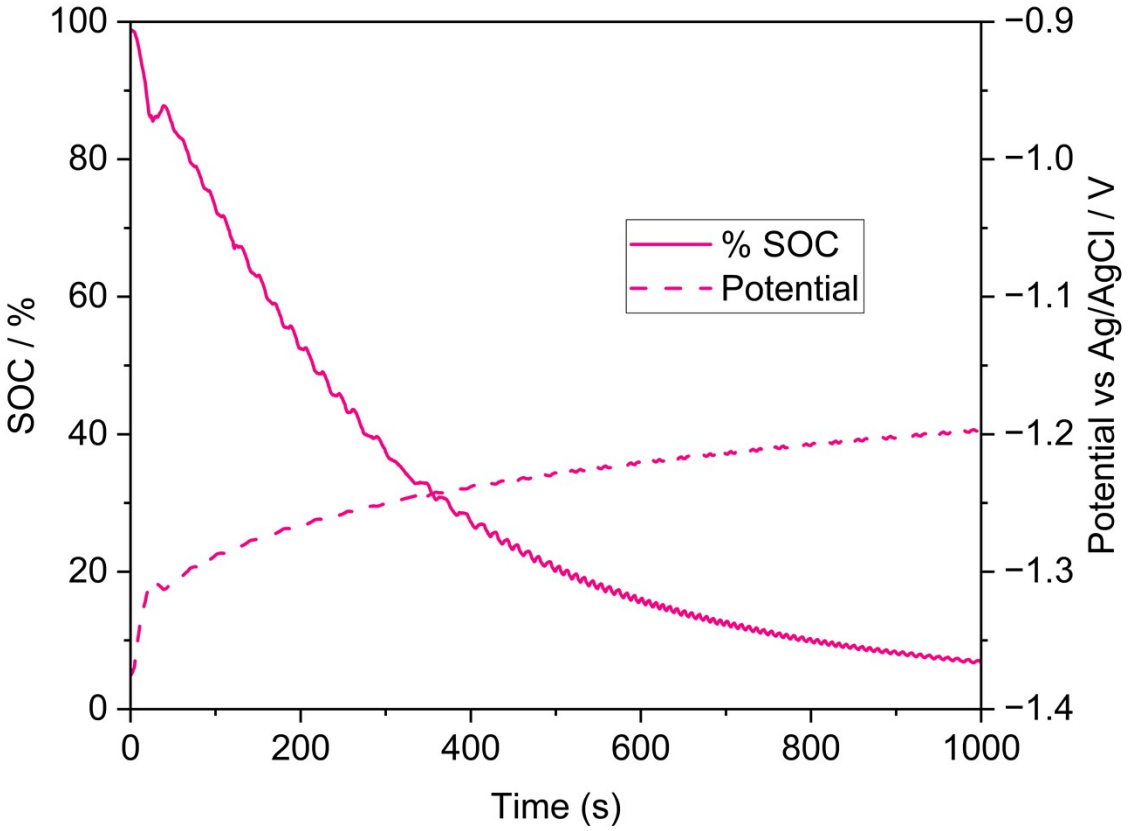

Figure S12. Open circuit potential and states of charge of solutions of 10 mM Cr(II)/(III) PDTA where the state of charge indicates the transformation of measured potentials vs a calibration curve obtained for known volume ratios of Cr(II)/Cr(III) PDTA.

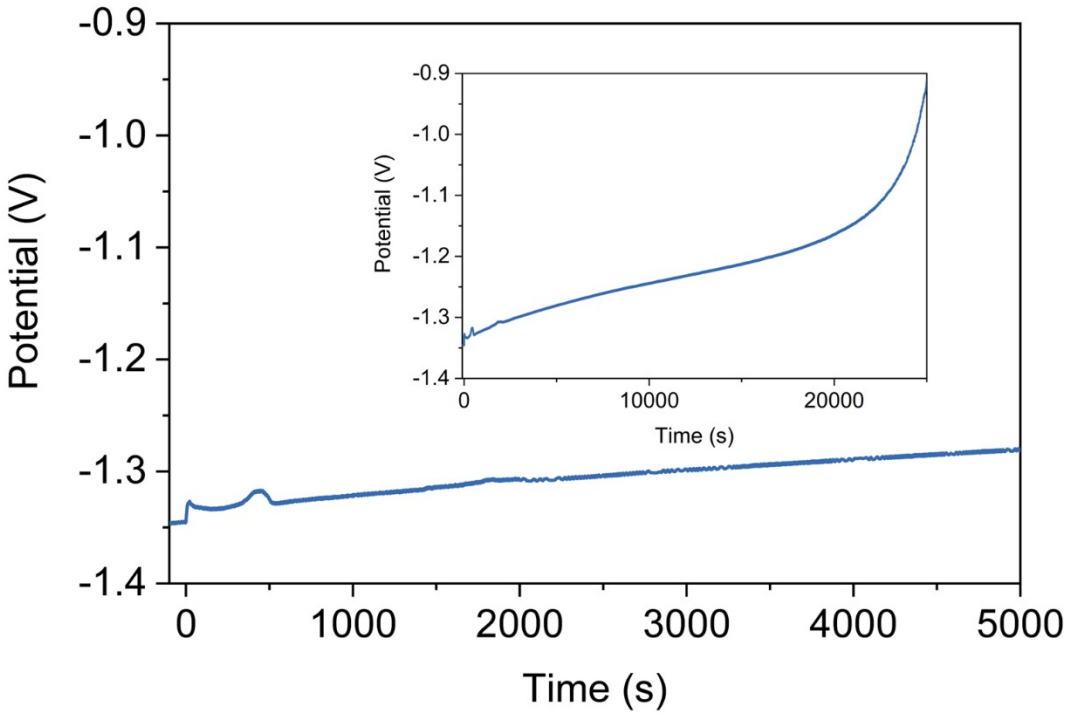

Fig S13. OCCP measurements for 10 mg SiO_2 concentration in presence of CrPDTA mediator. The mediator does not fully discharge until more than 25000 seconds instead of 5000 s, the time obtained for the lowest concentration of MoS_2.

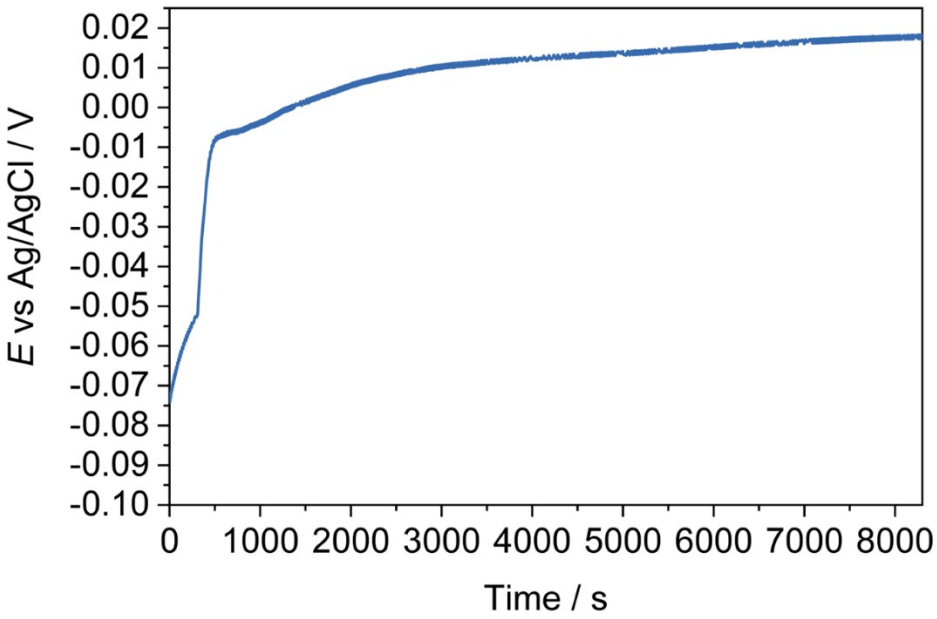

Figure S14. OCCP measurements for 10 MoS_2 concentration in absence of CrPDTA mediator.

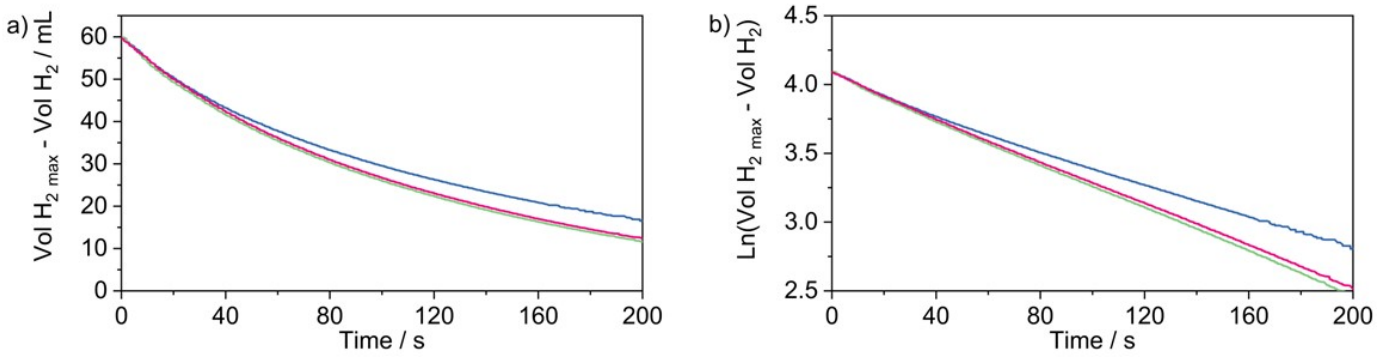

Figure S15. a) Graph of volume of H_2 produced over time normalised against expected volume (60 mL) for the first 200 seconds of reaction when 50 mL of 0.1 M Cr(II) PDTA is discharged over 25 mg of dispersed (by stirring) MoS_2. b) Natural log of a), where the high linearity suggests first order reaction kinetics with respect to mediator concentration.

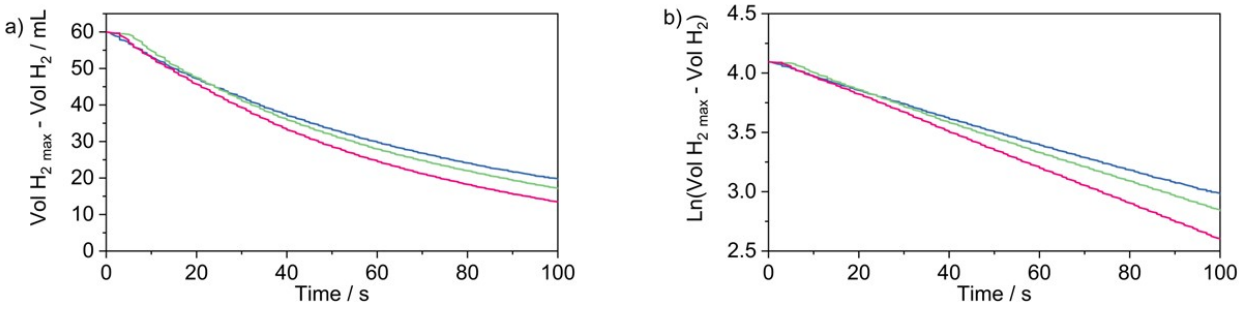

Figure S16. a) Graph of volume of H_2 produced over time normalised against expected volume (60 mL) for the first 100 seconds of reaction when 50 mL of 0.1 M Cr(II) PDTA is discharged over 50 mg of dispersed (by stirring) MoS_2. b) Natural log of a), where the high linearity suggests first order reaction kinetics with respect to mediator concentration.

Table S4. Table of hydrogen produced per unit of time for the reaction described in Figures S15-S16, as calculated from the volume of H_2 plots.

Volume of H_2 produced by unit of time	**50 mg**	**25 mg**
Run 1	6.83	5.23
Run 2	6.69	6.33
Run 3	7.13	5.54
Average (mean) apparent rate constant k_{app} (s^{-1})	6.8833	5.7000
Standard error (absolute)	0.1060	0.26737
Standard error (percentage)	1.5%	4.7%
$mLg^{-1}s^{-1}$)	13.76667	22.8

Table S5. Table of apparent rate constant calculations for the reaction described in Figures S15-S16, as calculated from the gradient of the ln plots.

Kinetic parameters	**50 mg**	**25 mg**
Run 1	0.0112	0.00610
Run 2	0.0129	0.00792
Run 3	0.0153	0.00771
Average (mean) apparent rate constant k_{app} (s^{-1})	0.0131	0.00724
Standard error (absolute)	0.0010	0.00047
Standard error (percentage)	7.4%	6.5%

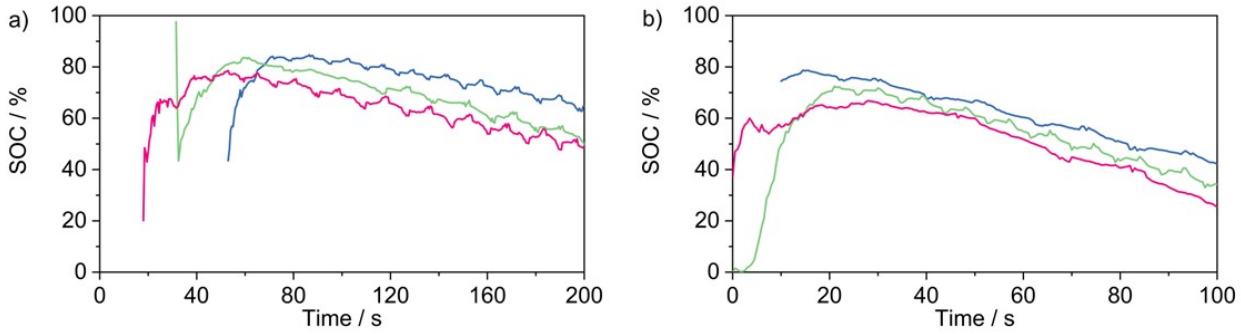

Figure S17. Plots of state of charge vs time for the experiments shown in Figure S15 a) and Figure S16 a), as calculated from continuous OCP measurement during discharge. It is clear from the noise and delayed response that the simultaneous measurement of H_2 volume and OCP needs improvement before it can be used together. The delay is due to the slow injection time. As a consequence, the circuit does not form until most of the volume is injected, but H_2 production begins immediately.

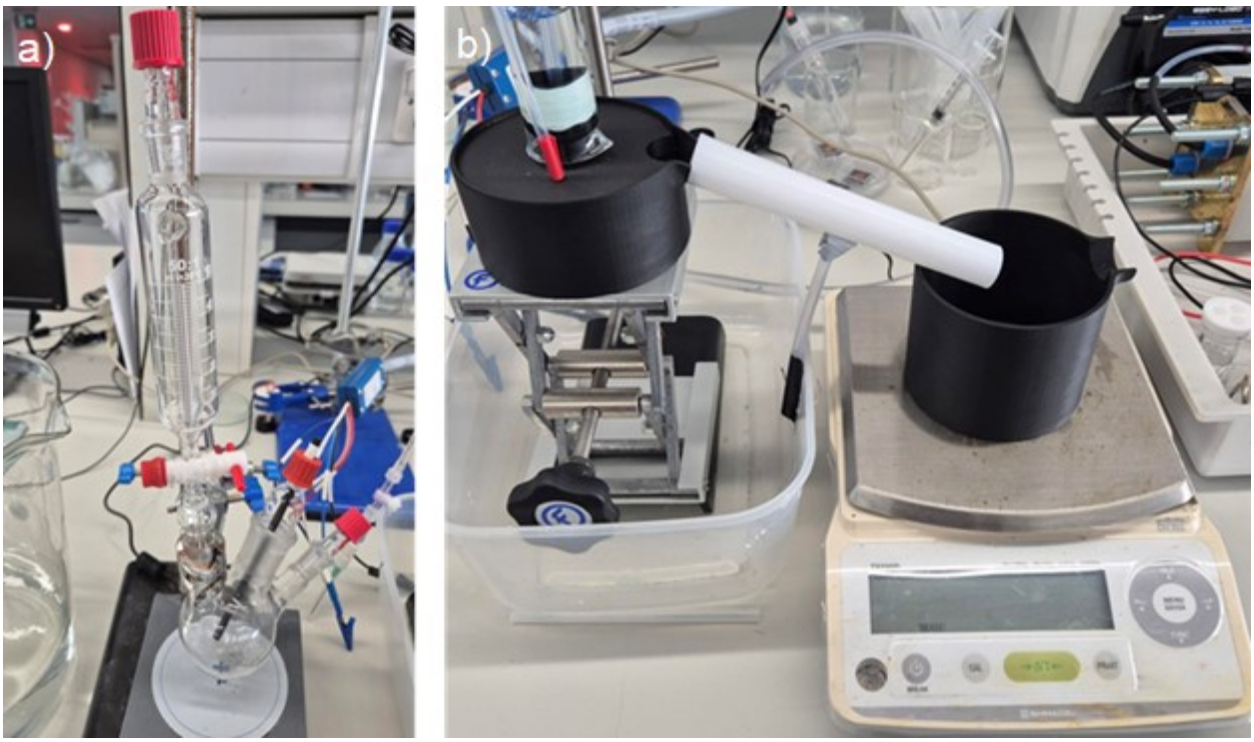

Figure S18. Images of the water displacement apparatus. Key items include a) pressure equilibrating funnel that allows for mediator injection without displacing additional water, electrodes for the collection of OCP data b) inverted cylinder for gas collection and water displacement, and mass balance for the continuous monitoring of displaced volume. The setup

was adapted from work by Brack et al.[9]. The main improvement in our system is that by minimising the surface are of water exposed to air, the induction volume required to overcome water surface tension can be made negligible.

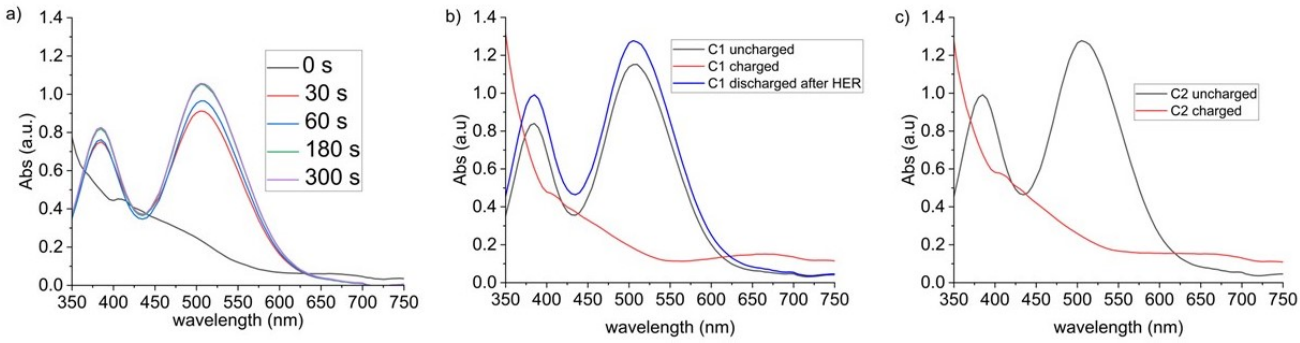

Figure S19. a) UV-Vis of CrPDTA discharge with MoS_2 in 5 mg/ml evaluated at indicated time intervals of 0 – 300 s. At 0 s the solution is green. Peaks corresponding to a colour change to red emerge almost immediately on addition of catalyst. b) UV-vis for a complete first cycle (C1). First, a peak at around 510 nm is obtained for the uncharged red/pink form of the mediator. When the mediator is charged, it turns green, with a wide band with a maximum at around 665 nm. After discharge over MoS_2, the characteristic peak at 510 nm is visible again. c) This discharged mediator can then be charged again (C2). In practice, this redox mediator has been cycled reversibly thousands of times in reports in the literature[10] for use in flow batteries with minimal changes.

Table S6. Faradaic yields obtained by evaluating conversion at 70% SOC, using volumetric mixing (100% SOC mediator is added to the corresponding 0% SOC mediator to yield a 70% SOC mixture) and galvanostatic charging aiming at theoretical 70% SOC

	Faradaic Yield (%)
volumetric mixing	89.08 ± 1.66
galvanostatic charging	80.58 ± 1.08

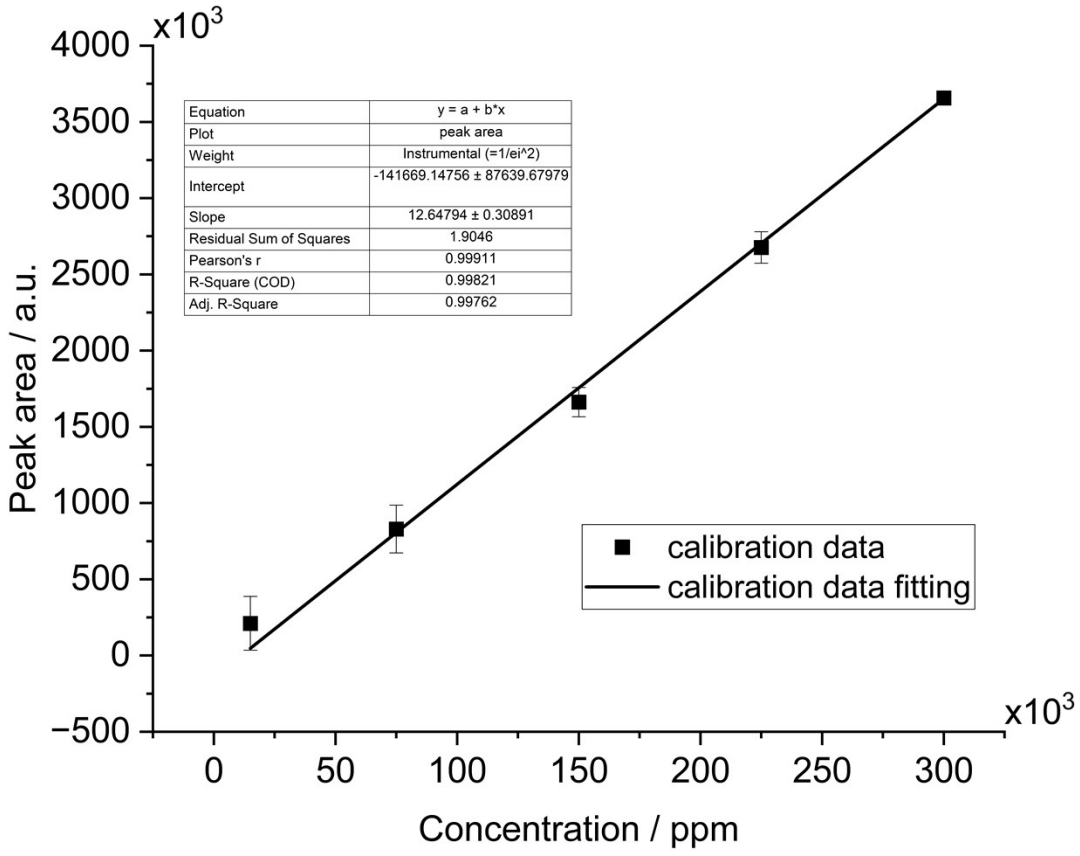

Figure S20. Gas chromatography calibration for hydrogen concentration. Samples were prepared from a calibration standard containing 300000 ppm H_2 with N_2 balance. Dilutions were performed in a glass syringe setup in N_2 to give concentrations of approximately 225000, 150000, 75000 and 15000 ppm. The calibration range has strong correlation, allowing for high confidence in the accuracy of determined concentrations.

Equations in the form y = mx + c were used to determine the concentration of H_2 in a real sample from the GC peak area;

Peak area = (12.167 × ppm) - 53123

Gas quantification and product analysis

To determine the faradaic yield for H_2, headspace gas was taken from the flask and analysed by gas chromatography. An aliquot of gas was collected in a gas-tight lock-in syringe. The sample was then directly injected into the GC inlet for separation. Using the above calibration plot, the concentration of H_2 was determined in ppm (molar ratio). It is assumed that 100% of all gaseous products were in the headspace, as H_2 is sparingly soluble in water.

The amount of H_2 in moles within the headspace was estimated;

$$Moles\ H2\ [mol] = \frac{Headspace\ concentration\ [ppm]}{10^6} \times Total\ moles\ of\ gas\ in\ headspace\ [mol]$$

where the ideal gas law was used to determine the total number of moles within the headspace;

$$Total\ moles\ of\ gas\ in\ headspace = \frac{Headspace\ pressure\ [Pa] \times Headspace\ volume\ [m^3]}{Ideal\ gas\ constant\ [J\,K^{-1}\,mol^{-1}] \times Temperature\ [K]}$$

By considering the electron stoichiometry, the amount of charge needed to form each product can be calculated;

$$Charge\ required\ [C] = Moles\ H2\ [mol] \times Electron\ stoichiometry \times Faraday\ constant\ [C\,mol^{-1}]$$

which can then be compared to the total charge passed;

$$Charge\ passed\ [C] = Concentration\ of\ mediator\ [M] \times Volume\ of\ mediator\ [L] \times Electron\ stoichiometry \times Faraday\ constant\ [C\,mol^{-1}]$$

to determine the faradaic yield as a quantum yield;

$$Faradaic\ yield = \frac{Charge\ required\ [C]}{Charge\ passed\ [C]} \times 100$$

Electrochemical set-up

Voltammetry electrodes and cells

Photographs of one carbon paste electrode are shown below. A plastic sheet is used to obtain a smooth surface on the carbon paste, not as a substrate for the catalyst. The cell-setup is a standard 3-electrode set-up using a Ag/AgCl reference electrode and carbon rod counter electrode.

Figure S21. Typical carbon paste electrode being polished on a plastic sheet. The

Electrolysis flow cell

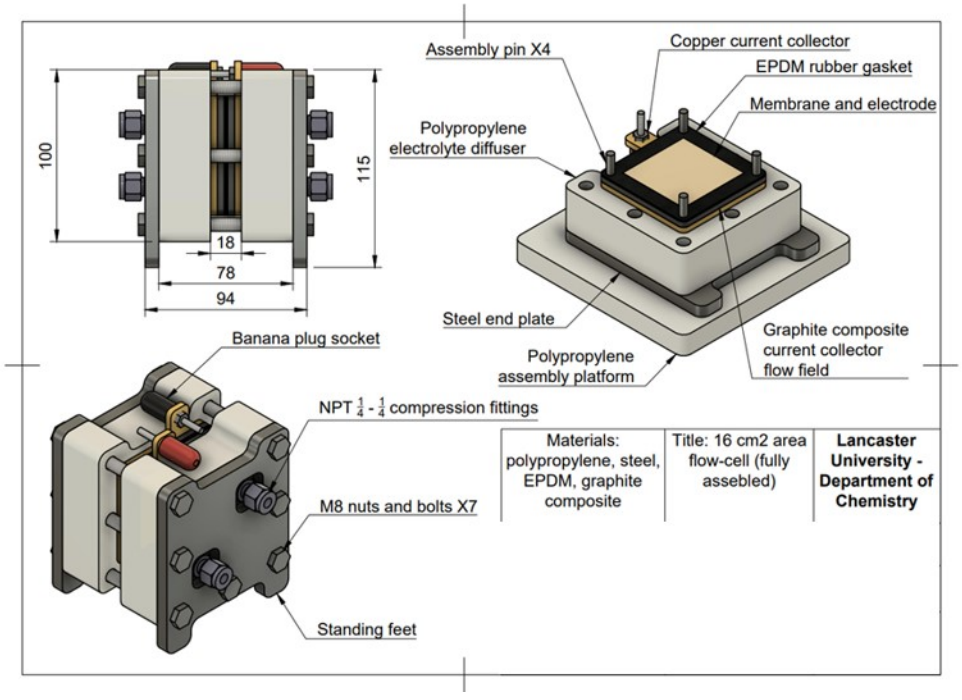

Figure S22: Schematic of the electrolysis cell used in this study.

Electrolysis of the redox mediators or water was undertaken using a 16 cm^2 two-electrode flow cell made in-house. The flow cell design is reported in other work by our group. [11]

In this study we operated the flow cell with two redox mediators, Cr PDTA and ferrocyanide, for the flow battery configuration. Or we modified the carbon felt electrode on the negative electrode (cathode during electrolysis) with a dispersion of MoS_2 as described in the Experimental section. We then operated the cell also versus ferrocyanide on the positive side, directly generating hydrogen in the catholyte stream. The hydrogen generated during electrolysis was collected in the water tank and sampled from the headspace or evolved to allow for the water displacement analysis.

References:

1. V. Amstutz, E. K. Toghill, F. Powlesland, H. Vrubel, C. Comninellis, X. Hu and H. H. Girault, *Energy & Environmental Science*, 2014, **7**, 2350–2358.
2. D. Reynard and H. Girault, *Cell Reports Physical Science*, 2021, **2**, 100556.
3. Y. Ji, F. Zhang, M. Zhou, J. Yu and Q. Wang, *International Journal of Hydrogen Energy*, 2020, **45**, 18888–18894.
4. F. Zhang, H. Zhang, M. Salla, N. Qin, M. Gao, Y. Ji, S. Huang, S. Wu, R. Zhang, Z. Lu and Q. Wang, *Journal of the American Chemical Society*, 2021, **143**, 223–231.
5. T. Liu, X.Wei, Z. Nie, V. Sprenkle, W. Wang, *Advanced Energy Materials*, 2016, **6**, 1501449.
6. E. Beh, D. de Porcellinis, R. Gracia, K. Xia, R. Gordon, M. Aziz, *ACS Energy Letters*, 2017, **3**, 639-644.
7. W. Ruan, J. Mao, S. Yang, C. Shi, G. Jia, Q. Chen, *Chemical Communications*, 2020, **56**, 3171-3174.
8. S. Waters, C. Davis, J. Thurston, M. Marshak, *Journal of the American Chemical Society*, 2022, **39**, 17753-17757.
9. P. Brack, S. Dann, K. G. Wijayantha, P. Adcock, S. Foster, *Journal of Visualized Experiments*, 2016, **114**, e54383
10. S. E. Waters, B. H. Robb, S. J. Scappaticci, J. D. Saraidaridis and M. P. Marshak, *Inorganic Chemistry*, 2022, **61,** 8752–8759.
11. M. Potter, D. E. Smith, C. G. Armstrong, K. E. Toghill*, EES Catal.* 2024, **2**, 379–388